J. Fluid Mech. (2007), *vol.* 574, *pp.* 365–391.
doi:10.1017/S0022112006004150 Printed in the United Kingdom

Suppression of the von Kármán vortex street behind a circular cylinder by a travelling wave generated by a flexible surface

CHUI-JIE WU[1,2]†, LIANG WANG[1,2] AND JIE-ZHI WU[3,4]

[1]Research Center for Fluid Dynamics, PLA University of Science and Technology, Nanjing 211101, China

[2]Institute of Hydraulics and Hydroelectrics, Hohai University, Nanjing 210098, China

[3]State Key Laboratory for Turbulence and Complex System, Peking University, Beijing 100871, China

[4]University of Tennessee Space Institute, Tullahoma, TN 37388, USA

(Received 21 October 2004 and in revised form 1 September 2006)

An advanced moving-wall control strategy to manage the unsteady separated flow over a circular cylinder is developed. A two-dimensional numerical simulation of the flow over the cylinder at $Re = 500$ based on diameter indicates that, when the downstream half of the cylinder surface is made flexible to form an appropriate travelling transverse wave, a 'fluid roller bearing' (FRB) is produced consisting of a row of vortices trapped by each wave trough, which can keep the global flow attached against a strong adverse pressure gradient, eliminating the vortex shedding and reducing the average drag by 85 %. Physically, the FRB serves as a sheath to effectively inhibit the momentum–energy exchange between the thin fluid layer adjacent to the wall and the main stream, so that the wall layer is scaled only to the local wavelength and frequency and is independent of the global scales. Therefore, the global adverse pressure gradient on the lee side of the cylinder no longer influences the near-wall flow, and the common root cause of flow separation is removed. The input power for actuating the flexible wall is found to be 94 % of the power saving due to drag reduction.

1. Introduction

Viscous flow around a bluff body, in particular a circular cylinder, is a classic problem of fluid mechanics owing to its rich phenomena of fundamental interest and crucial importance in a wide variety of engineering applications; for recent comprehensive reviews see Roshko (1993), Williamson (1996), and Zdravkovich (1997, 2002).

Bluff-body flow control has become one of the main concerns in various flow control problems. In this paper we report results from our two-dimensional numerical experiment on active open-loop control of flow over a circular cylinder in incompressible flow, at Reynolds numbers $Re = 500$, 2000 and 5000 based on the diameter. The control is achieved by producing a travelling wave on the rear part of the cylinder as sketched in figure 1. The control completely eliminates or nearly eliminates (for $Re \leqslant 2000$ or $Re = 5000$, respectively) the von Kármán vortex street behind the cylinder, changes the flow there from an oscillating wake to nearly steady and irrotational, and reduces the drag by 85 %. The benefit from the drag reduction is larger than the hydrodynamic power consumption for activating the flexible wall.

† Author to whom correspondence should be addressed: cjwu@jlonline.com or cj_wu@163.com

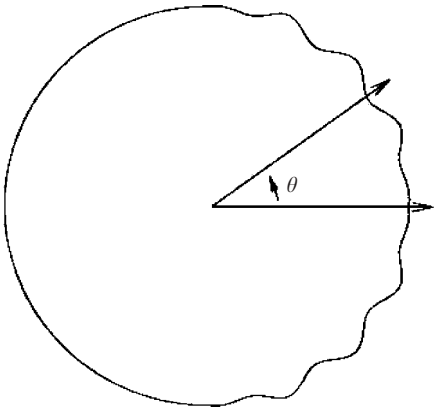

FIGURE 1. Cylinder with a flexible TTW wall.

Using a flexible wall to produce a travelling wave for flow control is a development of moving-wall control. It is appropriate here to briefly review various moving-wall control strategies applied to bluff-body flows. The key flow structures to be controlled in such a flow at large Reynolds numbers are highly unsteady attached and separated shear layers. While on a stalled airfoil a localized unsteady excitation near the separation point can effectively control the global flow field (e.g. Wu *et al.* 1998), on a circular cylinder the separation point has appreciable time-dependent movement, and a distributed control device becomes necessary. As has long been known, installing a piece of tangentially moving wall to reduce the shearing can considerably suppress the flow separation from a smooth surface, see e.g. the reviews of Modi (1997, 2000). Patnaik & Wei (2002) studied numerically the effect of this kind of control on the flow over a D-shaped cylinder by installing a pair of rollable cylinders at two edges of the cylinder to input angular momentum to the flow field. The von Kármán vortex street can thereby be alleviated.

Controlling a shear flow by a uniform wall tangential motion as in the above examples can be directly interpreted in terms of the input of momentum or angular momentum, but is almost unrealizable (with rare exceptions; see Modi 2000). An alternative and more advanced strategy uses an oscillating wall to produce *forcing waves*. The underlying physics of flow control by waves has great variety, one fundamental mechanism being that a shear flow is inherently associated with a very rich spectrum of instability and receptivity modes (e.g. Ho & Huerre 1984), so that it is possible to excite and enhance certain favourable modes (depending on the control purpose) and suppress other unfavorable ones with very small power input (Wu, J. Z., Vakili & Wu 1991). In this category, the oscillatory moving wall (e.g. an oscillating flap, figure 2*a*) has been widely used as a means of control.

For distributed oscillating-wall control, if the flow is basically two-dimensional, the wall may oscillate either tangentially to produce a longitudinal wave (LW) that does not alter the wall geometric shape (figure 2*b*, *c*), or normally to produce a transverse wave (TW) like that shown in figure 1 and figure 3 below, which changes the wall geometry dynamically.† While the LW moving wall is a direct extension of aforementioned uniform tangentially moving wall, the TW moving wall represents

† In fully three-dimensional flow, a flexible wall with tangential oscillation could also produce a transverse wave.

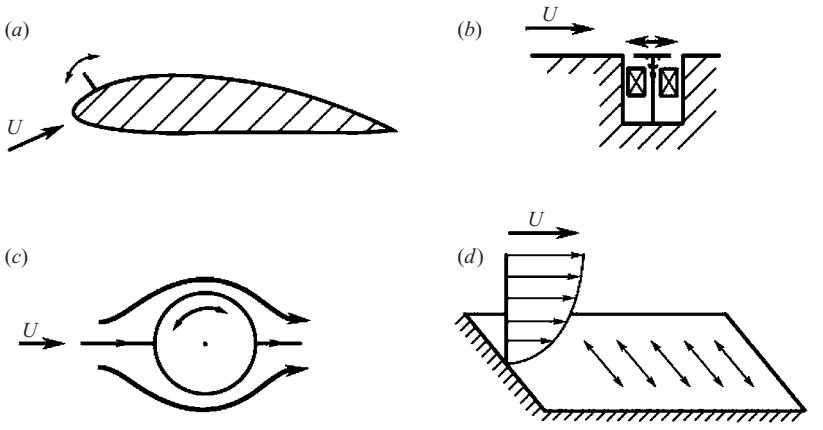

FIGURE 2. Sketches of shear flow control by various oscillating moving walls: (*a*) oscillating flap (cf. Zhou 1992); (*b*) locally and tangentially oscillating wall; (*c*) globally and tangentially oscillating wall; (*d*) spanwise standing or travelling wave produced by oscillating or flexible wall. These figures are based on the ideas of Zhou (1992), Wu, X. H., Wu & Wu (1991), Taneda (1978), and Zhao *et al.* (2004), respectively.

a new type of control strategy that will be addressed in detail below. Within each type, one may further distinguish standing waves and travelling waves. Generically, the latter are more effective and have wider potential applications than the former, because conceivably they involve more control parameters corresponding to richer physics and greater flexibility.

The elegant flow visualization experiments of Taneda (1978) made an important contribution to both LW and TW distributed moving-wall controls. In one experiment, Taneda showed that the vortical wake of a circular-cylinder flow at $Re = 35$ can be completely eliminated by the rotary oscillation of the cylinder (figure 2*c*) with amplitude of 45° and Strouhal number (based on radius) about 3.0 (a standing wave). A simple theory was proposed by Wu, Wu & Wu (1993) to quantitatively interpret this result as a finite-amplitude streaming effect of vorticity creation at boundary. This rotary-oscillation control has been explored at larger Reynolds numbers (for a literature review see Bergman, Cordier & Brancher 2006). In a numerical study of circular-cylinder flow control at $Re = 200$, Bergman *et al.* let the upstream part of the cylinder surface make a sinusoidal rotary oscillation and found that the control can produce a reverse Kármán vortex street and reduce the drag more efficiently than with the whole cylinder in rotary oscillation. In different circumstances, standing and travelling LW moving-wall controls have been used to reduce turbulent skin friction (e.g. Karniadakis & Choi 2003; Zhao, Wu & Luo 2004), which is another major field in which distributed control devices are necessary (figure 2*d*).

In a different visualization experiment, Taneda (1978) showed that an oscillating wall, which produces a *transverse travelling wave* (TTW) with an appropriate phase speed and sufficiently large amplitude, can trap a stable row of vortices at the wave troughs as sketched in figure 3(*a*). A similar result was independently obtained by Savchenko (1980). Thus, if a conventional boundary layer could be replaced by such a vortex row, the fluid layer between the main stream and solid wall would be changed from a 'sliding bearing' to a 'roller bearing', implying much smaller drag. This innovative phenomenon was explained by Wu *et al.* (1990) using a simple theory for two-dimensional flow over an infinitely extended TTW (an axisymmetric counterpart

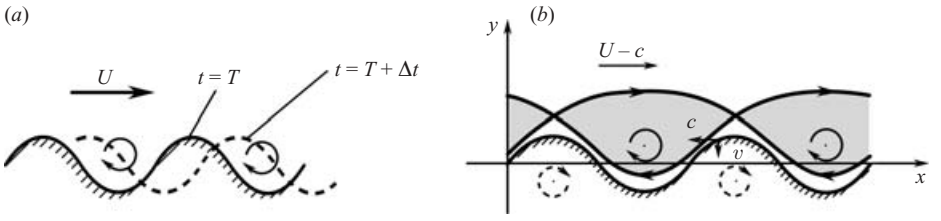

FIGURE 3. Sketch of vortex trapping by a TTW: (*a*) viewed in laboratory frame of reference, (*b*) viewed in a frame of reference fixed to the wave. Image vortices are denoted by dashed lines.

of the theory was later constructed by Yang & Wu 2005). Wu *et al.* examined the problem in the frame of reference moving with the wave, in which the flexible wall makes tangential motion only, toward the upstream direction; see the sketch of figure 3(*b*). The velocity induced by each trapped vortex between the vortex and the wall is also toward upstream, and hence with weaker shear than in a conventional boundary layer. Given the wave pattern and amplitude, the theory yields a critical wave speed at which the mean shear vanishes in the fluid layer adjacent to the wall. Once this happens, the flow enters a natually periodic state and the total drag on the wall approaches zero. This theoretical prediction was confirmed by a numerical computation reported in Wu & Wu (1996).

Wu, Xie & Wu (2003) introduced the name *fluid roller bearing* (FRB) for the key mechanism of the TTW control. They conducted a numerical FRB experiment with a finite-length TTW with a small number of peaks and troughs and then made a two-dimensional Reynolds-average Navier–Stokes simulation of the control experiment on a NACA-0012 airfoil at the stall angle of attack and $Re = 10^6$, where only the front part of the upper surface was set up to generate a TTW with only three peaks and troughs of variable amplitude (the maximum amplitude was 2.5 % chord length). It was found that the large-scale separated flow is suppressed, the lift is greatly enhanced and, except for the slight oscillation caused by the TTW, the forces and moment are time-independent. This work provided the first evidence that a finite-length TTW with only a few peaks and troughs can produce a very stable FRB effect even under a strong adverse pressure gradient. Of course, producing a TTW is not possible with a rigid wall; but it might have been commonly done by flying and aquatic animals for tens of thousands years. For example, figure 4 (from Hertel 1966) shows two photos of a dolphin before lunging out of the water and swimming at high speed, which shows a series of skin waves on the bodies; however, no motion pictures are known to the present authors to judge whether the waves were travelling. We believe that, as a result of the rapid development of smart materials and artificial muscles, TTW control will find engineering applications in the near future.

So far no theory is available to predict the optimal parameters for controlling the complex flow on a curved baseline contour by the finite-length TTW and FRB mechanism. Qualitatively, the results that have been previously found are as follows. First, both LW and TW produced by a moving wall can radically alter the vorticity creation at the wall and the near-wall shear flow. The effect on vorticity creation by LW control was addressed by Wu *et al.* (1993) and Zhao *et al.* (2004). The effect on near-wall flow by both LW and TW was discussed by Wu *et al.* (2005*b*) in terms of the fluid kinematics adjacent to a deformable surface, especially the change of the

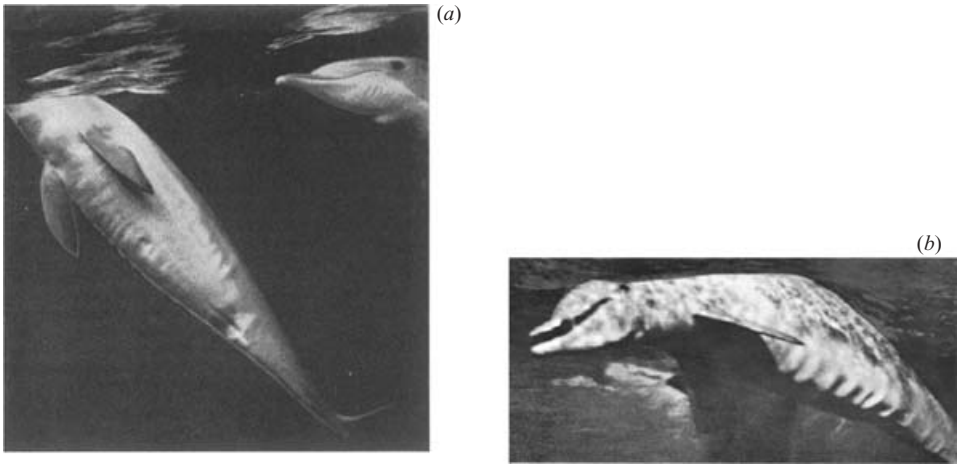

FIGURE 4. The skin waves on high-speed dolphins' bodies: (*a*) before lunging out of water, (*b*) high speed swimming.

fluid strain-rate tensor (along with the stretching and shrinking of the principal axes) due to the wall deformation.

Second, specifically for an FRB produced by TTW, each wave–trough vortex must come from the rolling up of the shear layer separating from the upstream wave peak. This implies two requirements. One is that the shear layer has to be sufficiently thin as otherwise it would hit the next wave peak before rolling up, with even poorer fluid-dynamic performance than a rigid baseline wall. Thus, the Reynolds number based on wavelength has to be sufficiently large. The other is that the flow has to separate and reattach periodically, and hence the ratio of wave amplitude to wavelength cannot be too small.

The present two-dimensional numerical study is a continuation of the work of Wu *et al.* (2003), from a fairly streamlined airfoil to a more bluff circular cylinder. In § 2 we define the TTW used in the control and discuss the parameter selection. The numerical method is outlined in § 3. We then present the major control results in § 4. An extensive physical discussion on why the FRB can work under a strong adverse pressure gradient is given in § 5. The dependence of the FRB control effect on the TTW parameters and the Reynolds number is discussed in § 6, followed by concluding remarks.

2. Control method formulation and parameters

Since unlike the TTW control of stalled airfoil flow studied by Wu *et al.* (2003), the flow we study separates from the lee side of the circular cylinder, we make the rear part of the cylinder surface flexible. A TTW is introduced that is symmetric with respect to the x-axis (the oncoming free-stream direction), so in formulating the control method it suffices to consider the upper part of the flow only. In polar coordinates (r, θ) with origin at the the cylinder centre and the ray $\theta = 0$ along positive x-direction, to be consistent with the convention that the streamwise coordinate increases as the fluid moves downstream, we define $\alpha = \pi - \theta \in [0, \pi]$ so that $\alpha = 0$ at the front stagnation point of the baseline cylinder and increases clockwise (i.e. streamwise). On the baseline cylinder we introduce the right-hand orthonormal triad $(\boldsymbol{e}_\alpha, \boldsymbol{e}_r, \boldsymbol{e}_z)$, which are tangent and normal to the cylinder, and normal to the flow plane, respectively.

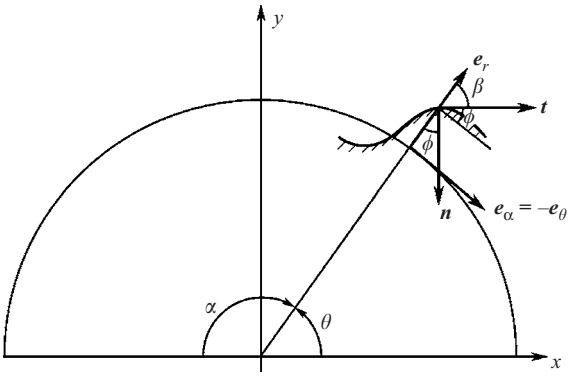

FIGURE 5. Geometric relations for a cylinder with a flexible TTW wall.

Let a material point $\boldsymbol{X} = r\boldsymbol{e}_r$ of the TTW wall perform a periodic radial motion (cf. figure 1)

$$r = r_0 + A(l)\cos[k(l - ct)], \quad k = \frac{2\pi}{\lambda}, \quad l = r_0\alpha, \tag{2.1}$$

where r_0 is the radius of the baseline cylinder, A is the amplitude, l is the arclength along the cylinder, and k, λ and c are the wavenumber, wavelength, and phase speed, respectively. The circular frequency is $f = kc$. By (2.1), the Lagrangian velocity and acceleration of the material point on the TTW are

$$\boldsymbol{u} = \boldsymbol{X}_{,t} = \boldsymbol{e}_r r_{,t} = \boldsymbol{e}_r f A(l)\sin(kl - ft), \tag{2.2}$$

$$\boldsymbol{a} = \boldsymbol{X}_{,tt} = \boldsymbol{e}_r r_{,tt} = -\boldsymbol{e}_r f^2 A(l)\cos(kl - ft). \tag{2.3}$$

In order to connect smoothly with the fixed part of the cylinder surface, we let the amplitude of the most upstream and downstream waves increase and decrease linearly with l, respectively. Thus, let N be the number of waves on the upper surface and $\hat{A}$ be the maximum amplitude, and denoting $l' = r_0(\alpha - \pi/2)$, we specify

$$\frac{A(l)}{\hat{A}} = \begin{cases} \dfrac{l'}{\lambda} & \text{for } 0 \leqslant l' \leqslant \lambda, \\ 1 & \text{for } \lambda \leqslant l' \leqslant (N-1)\lambda, \\ N - \dfrac{l'}{\lambda} & \text{for } (N-1)\lambda \leqslant l' \leqslant N\lambda. \end{cases} \tag{2.4}$$

The circular cylinder with a pair of upper and lower TTW sections so constructed, with $N = 4$, is shown in figure 1 and will be referred to as the "*TTW cylinder*".

Moreover, for later use, on the TTW wall we introduce a right-hand orthonormal triad $(\boldsymbol{n}, \boldsymbol{t}, \boldsymbol{e}_z)$, where $\boldsymbol{n}$ is the unit normal vector pointing into the body, and $\boldsymbol{t}$ is the unit vector tangent to the wall, see figure 5. Let ϕ be the angle from $\boldsymbol{e}_\alpha$ to $\boldsymbol{t}$ (so the positive direction of ϕ increment is counterclockwise), and s be the arclength of the TTW cylinder which increases along the $\boldsymbol{t}$-direction, so that

$$\tan\phi = \frac{\mathrm{d}r}{r_0\mathrm{d}\alpha} = \frac{\mathrm{d}r}{\mathrm{d}l} = A'(l)\cos\chi - Ak\sin\chi, \quad \chi \equiv kl - ft, \tag{2.5}$$

$$\mathrm{d}s = \mathrm{d}l\cos\phi + \mathrm{d}r\sin\phi = r_0\mathrm{d}\alpha\sqrt{1 + \tan^2\phi}. \tag{2.6}$$

The basis vectors $(\boldsymbol{n}, \boldsymbol{t})$, $(\boldsymbol{e}_\alpha, \boldsymbol{e}_r)$, and $(\boldsymbol{e}_x, \boldsymbol{e}_y)$ are related by

$$\begin{bmatrix} \boldsymbol{e}_\alpha \\ \boldsymbol{e}_r \end{bmatrix} = \begin{bmatrix} \sin\alpha & \cos\alpha \\ -\cos\alpha & \sin\alpha \end{bmatrix} \begin{bmatrix} \boldsymbol{e}_x \\ \boldsymbol{e}_y \end{bmatrix}, \tag{2.7}$$

$$\begin{bmatrix} \boldsymbol{n} \\ \boldsymbol{t} \end{bmatrix} = \begin{bmatrix} \sin\phi & -\cos\phi \\ \cos\phi & \sin\phi \end{bmatrix} \begin{bmatrix} \boldsymbol{e}_\alpha \\ \boldsymbol{e}_r \end{bmatrix} = \begin{bmatrix} \cos(\alpha-\phi) & -\sin(\alpha-\phi) \\ \sin(\alpha-\phi) & \cos(\alpha-\phi) \end{bmatrix} \begin{bmatrix} \boldsymbol{e}_x \\ \boldsymbol{e}_y \end{bmatrix}. \tag{2.8}$$

Thus, we also have

$$\partial_s = \boldsymbol{t}\cdot\nabla = r_0^{-1}\cos\phi\,\partial_\alpha + \sin\phi\,\partial_r. \tag{2.9}$$

Since these is no physical theory to provide quantitative guidance for numerical experiment with finite-length TTW on a curved baseline contour, the choice of optimal parameters was the most difficult part of our study and had to be made on a trial-and-error basis. A large number of numerical tests with different parameters were performed. Generically, for increasing Re, N and c should increase too, but $\hat{A}$ should decrease. Hence, a much denser grid is necessary. However, the most crucial parameter is the relative phase speed c/U with U being the oncoming free-stream velocity, which could be relevant to the excitation of certain inherent modes of the shear layers mentioned in § 1. The FRB effect exists and appears to be stable only in a particular range of c/U. Many values of c/U have been tested, but in this paper only the results for a single value ($c/U = 4$) are presented.

We use the diameter $d = 2r_0$ of the baseline cylinder, the oncoming free-stream velocity U, and fluid density ρ to non-dimensionalize all variables. Sometimes we retain dimensional expressions for clarity. When the Reynolds number based on d, Re_d, is 500, we found the following dimensionless parameters to be optimal for the present TTW cylinder configuration: $c/U = 4.0$ (the wave travels downstream), $N = 4$, $\lambda = \pi/(4N)$, and $\hat{A} = 0.02$. Thus, the oscillating period is $T = \lambda/c = \pi/64$ and the corresponding Strouhal number based on diameter, $St_d = d/(UT)$, is 20.37. Note that the Strouhal number based on wavelength is simply c/U. The Reynolds number based on the wavelength, Re_λ, is 98.2, which is about the lowest value at which the FRB can be produced. Except in § 6, our results reported and discussed below are exclusively for this set of parameters.

3. Numerical algorithm

We used the finite-volume method provided by Ferziger & Peric (1999) to solve the two-dimensional version of the incompressible Navier–Stokes and continuity equations, in the following Cartesian-component ($i = 1, 2$) integral form:

$$\frac{\partial}{\partial t}\int_\Omega \rho u_i \,\mathrm{d}\Omega + \int_S \rho u_i u_n \,\mathrm{d}S = \int_S \tau_{ij} n_j \,\mathrm{d}S - \int_S p n_i \,\mathrm{d}S, \tag{3.1}$$

$$\int_S \rho u_n \,\mathrm{d}S = 0, \tag{3.2}$$

where Ω is the control volume, S is the control surface and τ_{ij} is the viscous stress tensor. A second-order implicit three-time-level scheme was used for integration in time. The surface integral in (3.1) is split into four control-volume (CV) face integrals approximated by the midpoint rule. As a result, the spatial precision of the algorithm is second order.

When the cell faces move, the conservation of mass (and all other conserved quantities) is not necessarily ensured if the grid velocities are used to calculate the mass fluxes.

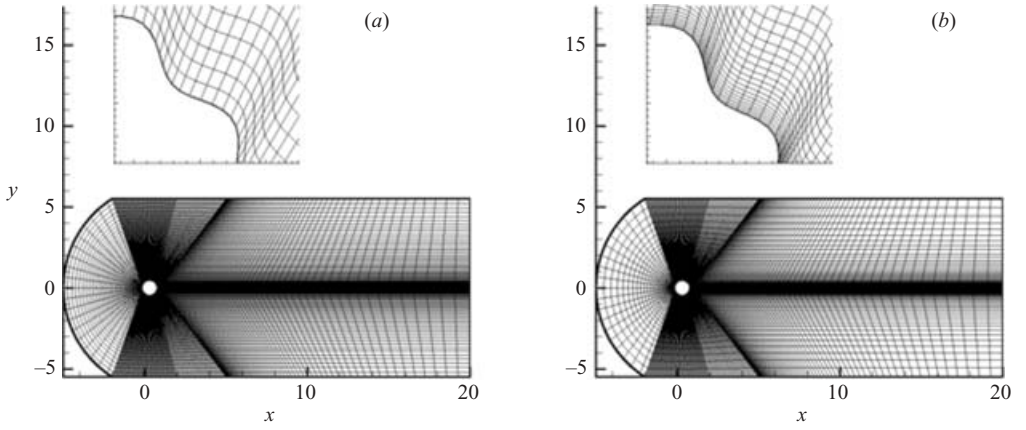

FIGURE 6. Computational grids: (*a*) Mesh 1, (*b*) Mesh 2.

Mass conservation can be obtained by enforcing the so-called space conservation law, which can be thought of as the continuity equation for zero fluid velocity:

$$\frac{\mathrm{d}}{\mathrm{d}t}\int_{\Omega}\mathrm{d}\Omega-\int_{S}\boldsymbol{u}_b\cdot\boldsymbol{n}\,\mathrm{d}S=0 \tag{3.3}$$

where $\boldsymbol{u}_b$ is the velocity of CV cell. This equation describes the conservation of space when the CV changes its shape and/or position with time. In discretized form, (3.3) becomes

$$\frac{(\Delta\Omega)^{n+1}-(\Delta\Omega)^{n}}{\Delta t}=\sum_{c}(\boldsymbol{u}_b\cdot\boldsymbol{n})_c S_c,\qquad c=e,w,n,s, \tag{3.4}$$

where $e, w, n,$ and s stand for the right, left, top and bottom faces of the cell, respectively. For the implicit Euler scheme, the discretized continuity equation becomes

$$\frac{(\rho\Delta\Omega)^{n+1}-(\rho\Delta\Omega)^{n}}{\Delta t}+\sum_{c}\dot{m}_c=0,\qquad c=e,w,n,s, \tag{3.5}$$

where $\dot{m}_c$ is the mass flux through a cell face c. The unsteady term has to be treated in a way consistent with the space conservation law. For incompressible flows, the contribution of the grid movement to the mass fluxes must cancel the unsteady term so that (3.2) is satisfied in the moving grid system. The validation and details of the algorithm can be found in Ferziger & Perić (1999), which includes standard convergence and grid refinement tests for similar bluff-body flow (Ferziger & Perić 1999, p. 253).

The above discretized equations were solved on a C-type uneven structured grid, and the computational domain is in the region $-5.0\leqslant x\leqslant 20.0$, $-5.5\leqslant y\leqslant 5.5$ in the x-, and y-directions, with the centre of the cylinder at $(0.308, 0)$, as shown in figure 6(*a*). The grid was 340×50, and the minimum grid interval normal to the wall was 0.016 (Mesh 1 of figure 6). The in-flow and out-flow conditions were imposed on the left and right boundaries, respectively. The free-slip condition was imposed at the top and bottom boundaries, and the no-slip condition was used on the cylinder surface. A uniform velocity distribution over the entire domain was taken as the initial computational condition.

A computation was conducted with the same 340×50 grid but much denser meshes near the TTW cylinder surface, the minimal normal mesh size being 0.003, as shown in figure 6(*b*), called Mesh 2, to test the grid effect on the simulation. The time

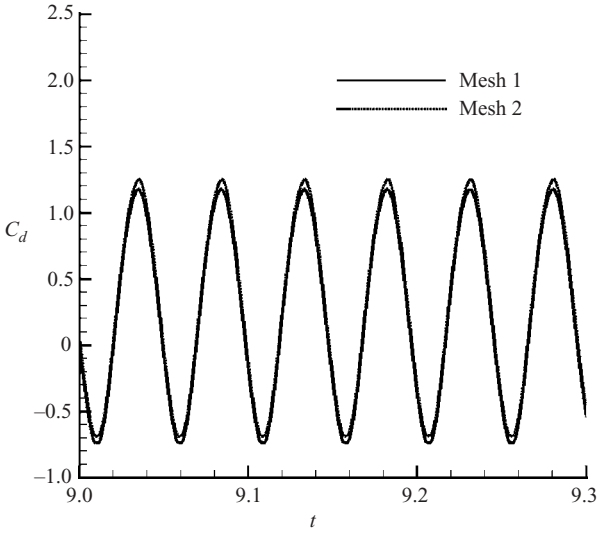

FIGURE 7. The time history of drag coefficient of the TTW cylinder (for definition see (4.4) below) for two meshes.

	St_d	C_d (avg.)	C_l (r.m.s.)
Current study	0.178	1.490	0.261
Lai & Peskin (2000) (numerical)	0.165	1.4473	0.3299
Dias & Majumdar (numerical)	0.171	1.395	0.283
Kim, Kim & Choi (2001) (numerical)	0.165	1.33	–
Zdravkovich (exp. as reported in Zdravkovich 1997)	0.165	1.40	–

TABLE 1. Comparison of several results for baseline-cylinder flow at $Re = 100$.

dependence of the drag coefficient C_d of the TTW cylinder at $Re = 500$ for both grids is shown in figure 7. The comparison indicates that at this Re Mesh 1 almost satisfies the desired grid-independence, and hence was adopted in most of our calculations. Mesh 2 was used in § 6 for higher Reynolds numbers.

For flow over the baseline cylinder at $Re = 100$, table 1 compares the result obtained by this numerical algorithm and those from an experiment and other numerical simulations, indicating that our result is reasonably good. While our computed St_d is somewhat larger than most results in the table, it is quite close to the numerical result of Dias & Majumdar (cited by Tseng & Ferziger 2003). Then, for $Re = 500$, from figure 9 below we find that the vortex shedding period in baseline-cylinder flow is 4.4215, corresponding to $St_d = 0.2262$, which differs from the 0.225 calculated by Henderson (cited in figure 21 of Williamson 1996) by only 0.53 %.

4. Control effect and power consumption

We now report the control effects of a TTW for $Re_d = 500$ for the optimal parameters given above, including the flow field, the force and pressure distributions, and the power consumption for activating the TTW wall. The units in the following figures are dimensionless.

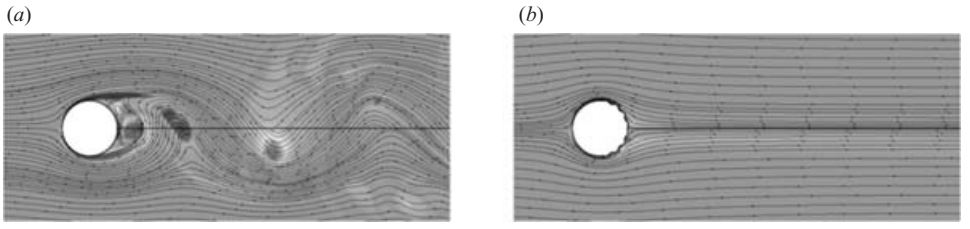

FIGURE 8. Streamlines and vorticity contours of (*a*) baseline and (*b*) TTW cylinders at $t = 50.0$.

First, let the TTW wall be activated at $t = 0$. Figure 8 compares the instantaneous streamlines and vorticity contours of the baseline- and TTW-cylinder flows at dimensionless time $t = 50$. The von Kármán vortex street clearly seen in the former is completely eliminated by the TTW. In fact, after the starting vortices are shed downstream, except for the small-scale controlled separation at each wave trough (see figure 27(*b*) below), no global flow separation occurs on the TTW cylinder surface. The large-scale unsteady separated vortical flow is broken up into the small-scale FRB flow. Thus, with the parameters chosen above, the TTW makes the bluff cylinder into a streamlined body, carrying an energetic attached flow able to overcome a very strong adverse pressure gradient.

The surface stress (pressure force plus friction force) on the TTW wall is given by $p\boldsymbol{n} + \boldsymbol{\tau}_w$, where

$$\boldsymbol{\tau}_w = \mu\omega\boldsymbol{n} \times \boldsymbol{e}_z = -\mu\omega\boldsymbol{t} = \tau_w\boldsymbol{t} \tag{4.1}$$

is the skin friction with ω being the vorticity. Thus, letting the total arclength of the upper surface be s_u and using (2.8), the total lift and drag on the upper surface are found to be

$$L = \boldsymbol{e}_y \cdot \int_0^{s_u} (p\boldsymbol{n} - \mu\omega\boldsymbol{t})\,\mathrm{d}s = -\int_0^{s_u} [p\sin(\alpha - \phi) + \mu\omega\cos(\alpha - \phi)]\,\mathrm{d}s, \tag{4.2}$$

$$D = \boldsymbol{e}_x \cdot \int_0^{s_u} (p\boldsymbol{n} - \mu\omega\boldsymbol{t})\,\mathrm{d}s = \int_0^{s_u} [p\cos(\alpha - \phi) - \mu\omega\sin(\alpha - \phi)]\,\mathrm{d}s, \tag{4.3}$$

where ϕ and $\mathrm{d}s$ are determined by (2.5) and (2.6). The lift and drag on the upper surface of the baseline cylinder are simply special cases of (4.2) and (4.3) with $\phi \equiv 0$ and $\mathrm{d}s = r_0\,\mathrm{d}\alpha$. With our non-dimensionalization convention, the coefficients of lift and drag are simply

$$C_l = \frac{L}{\frac{1}{2}\rho U^2 d} = 2L, \quad C_d = \frac{D}{\frac{1}{2}\rho U^2 d} = 2D. \tag{4.4}$$

Figure 9 shows the time history of C_l for the baseline and TTW cylinders. The TTW effectively inhibits the alternate vortex shedding and hence eliminates the lift. Note that the lift calculation was carried out until $t = 100$ (not fully shown in figures 9 and 10), when the C_l of baseline cylinder was observed to be well-converged.

Figure 10 shows the drag coefficient of the baseline and TTW cylinders. The time-averaged drag is reduced by 85.14 %, from 1.599 of the baseline cylinder to 0.238 of the TTW cylinder.

Figure 11 is a magnified plot of the time history of both C_l and C_d of the TTW cylinder, within a short time interval. The oscillation period is 0.0495, differing from the imposed TTW period $T = \pi/64$ by only 0.84 %. Therefore, the frequency of the TTW flow is locked onto the forcing frequency. The corresponding St_d is 20.20. This may be compared with the much smaller natural St_d of 0.226 of the baseline-cylinder

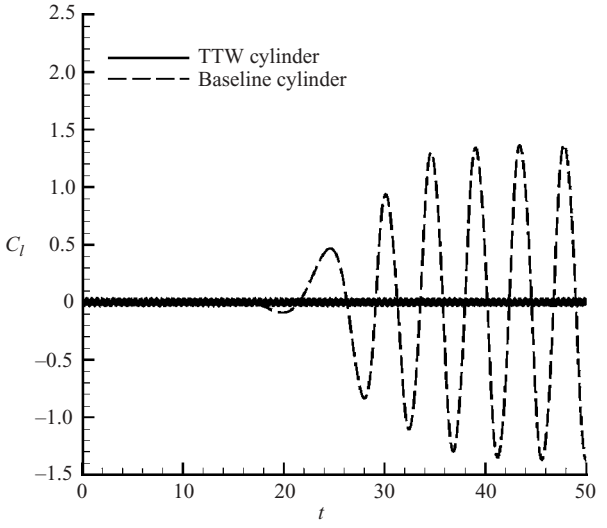

FIGURE 9. The lift coefficient of baseline and TTW cylinders.

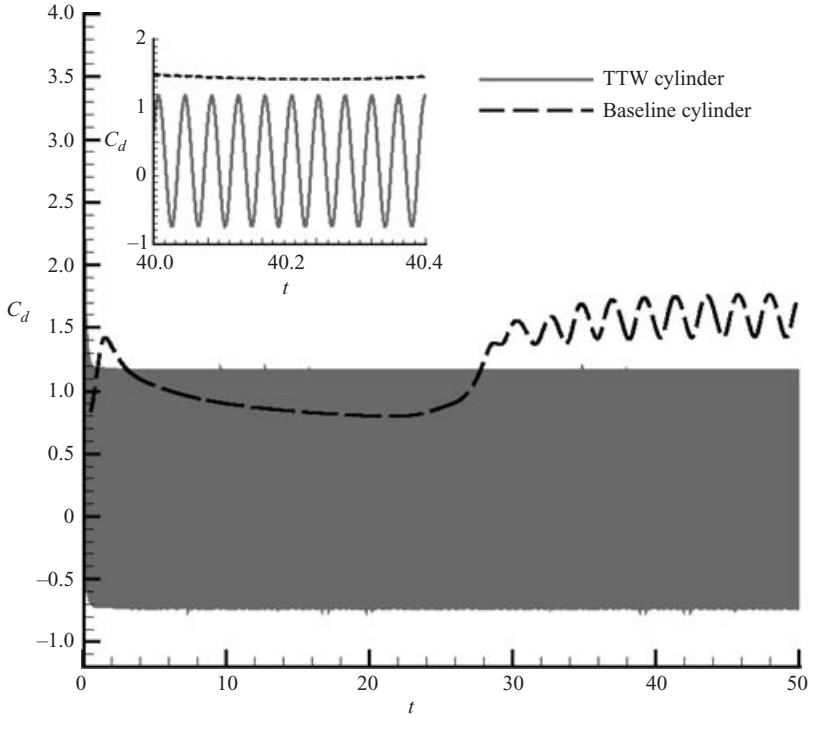

FIGURE 10. The coefficient of drag of baseline and TTW cylinders. The inset shows a magnified plot.

flow. Remarkably, although the average drag is dramatically reduced for the TTW cylinder, its oscillation amplitude is still quite large as seen in figures 10 and 11. The reason can be found from the next three figures. On each wave trough and peak, there is a maximum-pressure spot and a minimum-pressure spot, respectively (figure 12). Thus, the wave propagation must carry a very strong pressure fluctuation,

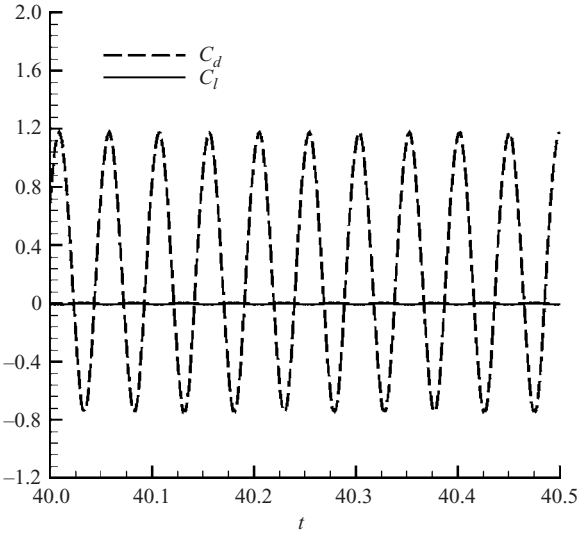

FIGURE 11. Local force acting on TTW cylinder.

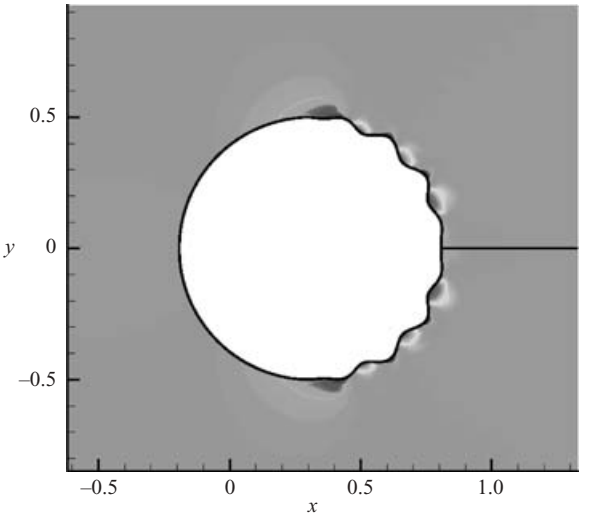

FIGURE 12. Pressure contours of TTW-cylinder flow at $t = 20.146$.

much stronger than the shear-stress fluctuation (see figures 13 and 14), which causes the observed significant drag amplitude.

Hydrodynamically, the power consumption for activating the TTW is the work done by the wall to overcome the pressure force and friction force. Let the total length of the TTW on the upper surface be L ($<s_u$); by (2.8) and (2.2) the power input is

$$P_{TTW}^{\mathrm{up}} = -\int_L u_r(p\cos\phi + \mu\omega\sin\phi)\,\mathrm{d}s. \tag{4.5}$$

But by (2.5) and (2.6)

$$\cos\phi\,\mathrm{d}s = r_0\,\mathrm{d}\alpha, \quad \sin\phi\,\mathrm{d}s = \frac{\mathrm{d}r}{\mathrm{d}l}r_0\,\mathrm{d}\alpha,$$

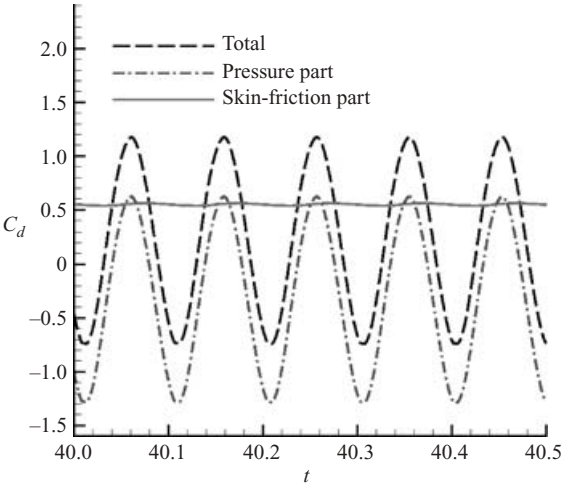

FIGURE 13. Total drag of TTW cylinder and the parts due to pressure and shear force.

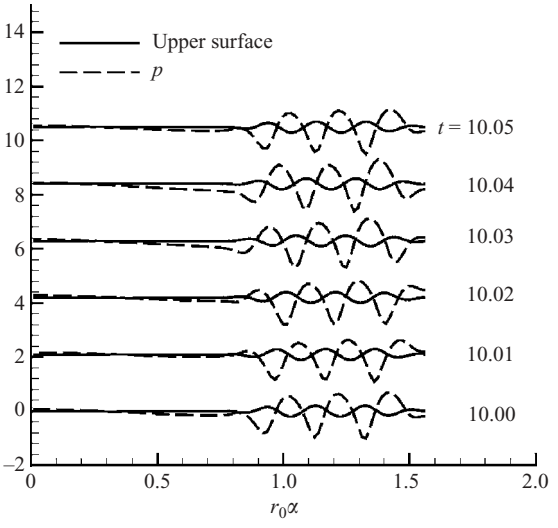

FIGURE 14. Pressure force on the upper surface of the TTW cylinder. For clarity, in this and the following time-evolution figures, the boundary vorticity flux and boundary vorticity are normalized by their respective maximum values, respectively; the TTW amplitude is amplified by 10 times; and the abscissas at different t are shifted from each other by 2.1.

where $\mathrm{d}r/\mathrm{d}l$ is given by (2.5). Hence, with $r_0 = 1/2$, on the upper surface, we have

$$P_{TTW}^{\mathrm{up}} = -\frac{f}{2}\int_{\pi/2}^{\pi} A(l)\sin\chi\{p + \mu\omega[A'(l)\cos\chi - kA(l)\sin\chi]\}\,\mathrm{d}\alpha, \tag{4.6}$$

with $\chi \equiv kl - ft$. Figure 15 shows the time history of this power input, from which we found that the power needed to overcome the pressure and friction forces is divided as 86 % and 14 %, respectively. Figure 16 shows the time history of the work needed on a small piece of the TTW wall centred at $\alpha_m = 3\pi/4$, i.e. computed from (4.6) but with α varying only in the interval $\alpha \in [\alpha_m - \delta, \alpha_m + \delta]$, where $\delta = \pi/200$. Note that

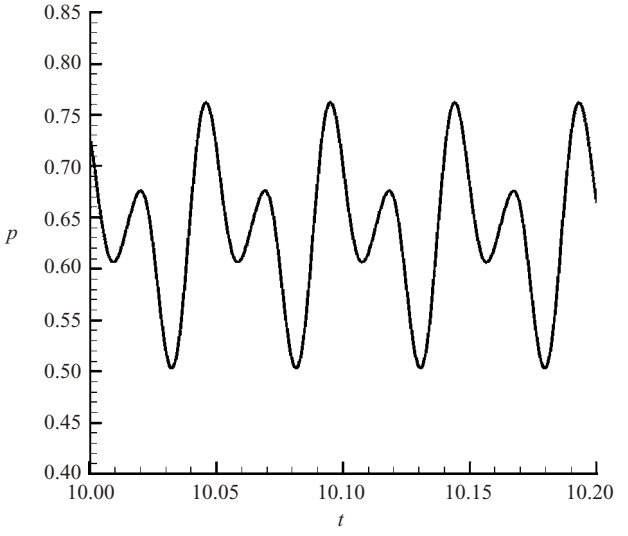

FIGURE 15. Total work needed by the TTW to overcome pressure.

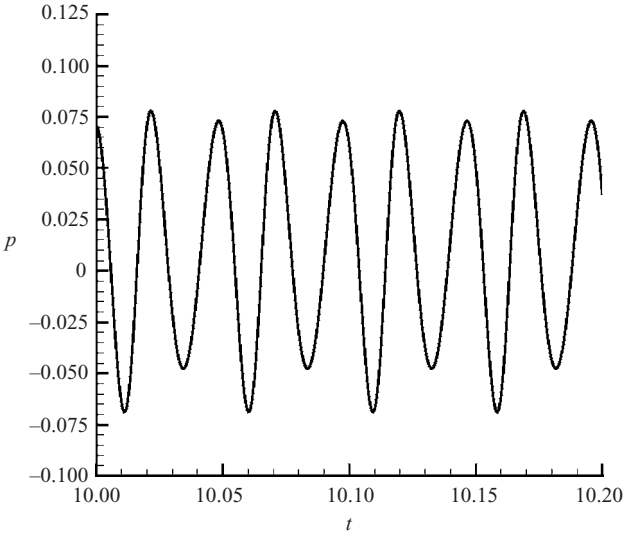

FIGURE 16. Work needed to overcome pressure at the middle point of the TTW wall.

although at this particular point the wall motion does both positive and negative work over time, figure 15 indicates that the required power input integrated over the TTW wall is always positive at any t. The mean power input over a time period T is

$$\overline{P}_{TTW}^{\mathrm{up}} = \frac{1}{T}\int_{T} P_{TTW}^{\mathrm{up}}\mathrm{d}t = 0.638. \tag{4.7}$$

The corresponding power input at the lower-surface TTW has almost the same time history and identical averaged value.

On the other hand, the averaged power needed to overcome the drag is $\overline{D}U$. Therefore, with (4.7) and (4.3), as well as $U = 1$, the ratio of the mean power consumption

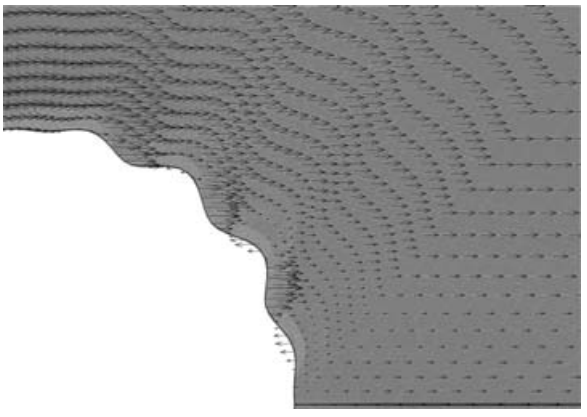

FIGURE 17. Distributed jets on the lee side of the TTW wall.

for driving TTW and the mean power savings due to the drag reduction is

$$\frac{2\overline{P}^{\mathrm{up}}_{\mathrm{TTW}}}{\overline{D}_{\mathrm{baseline}}-\overline{D}_{\mathrm{TTW}}}=\frac{1.276}{1.599-0.238}=93.8\,\%, \tag{4.8}$$

indicating a 6.2 % net saving. A few remarks are in order with respect to this value.

1. While in practical applications this saving looks quite small, the power consumption nevertheless compares reasonably with the distributed LW control for turbulent drag reduction (Zhao *et al.* 2004).

2. As will be demonstrated in § 5.4, this power consumption is much larger than that for activating the TTW in a flow without adverse pressure gradient. The benefit of TTW control over a fixed bluff body surface is not simply reducing the drag, but also other effects, such as the considerable alleviation of fluid-induced structure vibration and the recovery of the nearly steady irrotational flow downstream of the cylinder.

3. More importantly, in this computation the TTW cylinder was held fixed. If it is free in a fluid otherwise at rest, it will have a self-locomotive motion, possibly with a small mean thrust associated with distributed jets in the lee side of the TTW as shown in figure 17. Thus, (4.8) would also imply a propulsion efficiency $0.238/1.276=0.187$. If the motion is a constant translation, this efficiency is much lower than that of a TTW flat plate or thin airfoil, e.g. Wu, Pan & Lu (2005*a*), where $c/U=1$ is already nearly the wave speed needed to reach constant forward motion. This difference simply shows that due to the major power input needed to overcome the strong adverse pressure gradient, a TTW cylinder is by no means an optimal self-locomotive configuration. Nevertheless, because the distinction between the thrust and drag of a self-locomotive body such as a fish has not been clearly identified, taking (4.8) as only a drag-reduction efficiency would be an oversimplified viewpoint.

So far the results have been presented for the case with the TTW starting at the beginning of the fluid motion. It is of interest to see whether the TTW control can eliminate existing oscillating wake vortices. The answer is positive as confirmed by another test where the TTW was activated at $t=50$ after the von Kármán street is already well-established, see figures 18 and 19. At $t=55$ the oscillation in the near wake is almost eliminated, and at $t=61$ we obtain the same control effect as if the TTW were started at $t=0$. The animations of TTW control of circular-cylinder flow can be downloaded at http://turbulence.kmip.net/wavy-cyl-.tar.gz (14.5MB).

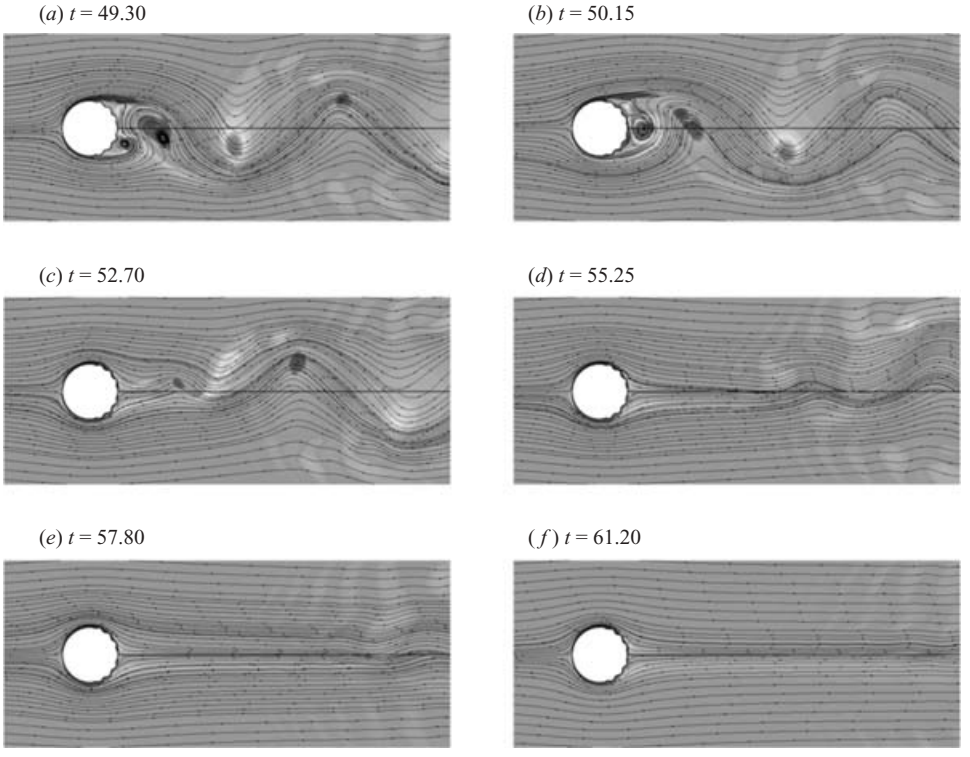

FIGURE 18. The flow evolution over a TTW cylinder, when the wave starts at $t = 50$.

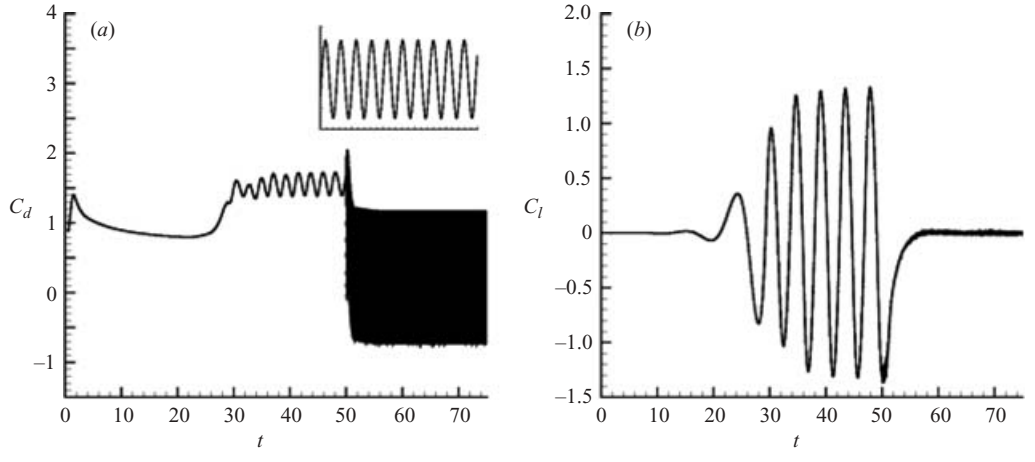

FIGURE 19. (*a*) Drag and (*b*) lift of a TTW cylinder, when the wave starts at $t = 50$. The inset in (*a*) is a zoom.

The TTW control effect can also be examined in a frame of reference fixed to the undisturbed fluid through which the cylinder moves with constant velocity $-\boldsymbol{U} = -U\boldsymbol{e}_x$. The instantaneous flow patterns at $t = 100$ for the baseline- and TTW-cylinder flows, with the wave turned on at $t = 0$, are compared in figure 20. The motion of the baseline cylinder from right to left clearly causes flow separation and vortex shedding, and thereby results in spontaneous oscillating forces on the cylinder.

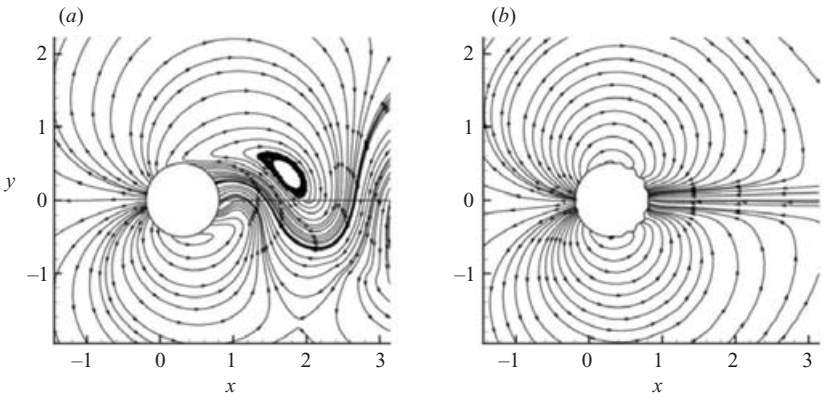

FIGURE 20. Relative flow fields of (*a*) baseline and (*b*) TTW cylinders at $t = 100$.

In contrast, the flow pattern for the TTW cylinder shown in figure 20(*b*) is similar to the non-circulatory, inviscid and potential doublet flow with up–down and fore–aft symmetry, along with zero lift and drag. The residual fore–aft asymmetry of the relative streamlines shown in figure 20(*b*) is caused solely by the rotational motion in the FRB.

5. FRB effect under adverse pressure gradient

As pointed out in § 1, the basic physical mechanism of the TTW control is the fluid roller bearing (FRB) effect. Although a complete predictive physical theory is still lacking, the remarkable ability of a finite-length FRB on a curved baseline surface to work against a strong adverse pressure gradient, as observed by Wu *et al.* (2003) and here, should have a clear physical interpretation, at least qualitatively. This issue is addressed below.

5.1. *Vorticity creation and near-wall flow locking to the TTW*

In a two-dimensional viscous flow, an adverse pressure gradient ($\partial p/\partial s > 0$) along a solid wall produces new vorticity at the wall that has opposite sign to the existing vorticity in the attached boundary layer, and eventually causes the boundary layer to separate. Therefore, the vorticity creation at the wall, due to the pressure gradient and the no-slip condition, should be the focus of our investigation. This creation process is measured by the boundary vorticity flux

$$\sigma = \nu \boldsymbol{n} \cdot \nabla \omega = \nu \frac{\partial \omega}{\partial n} \quad \text{on the wall,} \tag{5.1}$$

where $\boldsymbol{n}$ is the unit normal vector pointing out of the fluid as before. An application of the incompressible Navier–Stokes equation to the wall then yields

$$\sigma = \sigma_a + \sigma_p, \quad \sigma_a = a_s, \quad \sigma_p = \frac{1}{\rho}\frac{\partial p}{\partial s}, \tag{5.2}$$

where $a_s = \boldsymbol{a} \cdot \boldsymbol{t}$ is the wall tangential acceleration. The tangential components of $\boldsymbol{a}$ and ∇p on the wall form the two constituents σ_a and σ_p of the boundary vorticity flux, respectively. While σ_p is not directly controllable but is a synthetic global effect of the flow, σ_a is solely determined by our TTW design and independent of the flow.

We now examine the basic characteristics of the boundary vorticity flux on the upper-surface TTW wall, for the flow under the optimal-parameter condition found

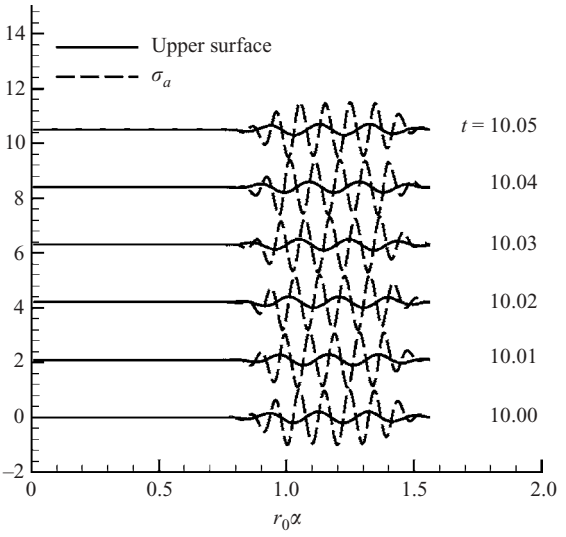

FIGURE 21. σ_a on the upper surface of the TTW cylinder.

in § 4. Consider σ_a first. From (2.4) and (2.8) we have

$$\sigma_a = a_r \sin\phi = -k^2c^2A(l)\cos[k(l-ct)]\sin\phi, \quad k = \frac{2\pi}{\lambda}, \tag{5.3}$$

where ϕ is determined by (2.5). For the chosen $\hat{A} = 0.02$ and $\lambda = \pi/16$ we have $A'(l) = O(\hat{A}/\lambda) \sim 0.1$, but $k\hat{A} = 0.64$, so that $\sin\phi \approx \tan\phi \approx -Ak\sin\chi$. Hence (5.3) can be approximated by

$$\sigma_a \approx \tfrac{1}{2}k^3c^2A^2(l)\sin 2[k(l-ct)], \tag{5.4}$$

having a period half that of the TTW. This feature is shown in figure 21 for a full TTW period. Equation (5.4) indicates that σ_a is most sensitive to the wavenumber k and speed c of the TTW, but less so to the maximum amplitude $\hat{A}$ due to its smallness. We have confirmed this through a large number of numerical experiments with various values of the parameters.

The positive and negative σ_a peaks cause the generation of counterclockwise and clockwise vorticity, respectively. However, as shown by Wu *et al.* (1990) and Wu & Wu (1996), since under the optimal condition the wall layer is isolated from the main-stream flow by the FRB, the flow shearing adjacent to the wall is much weaker than that in a boundary layer over a rigid wall. Therefore, the vorticity creation due to σ_a is not a strong mechanism in the control effect; rather, it is a byproduct of the TTW that directly captures the FRB row. Note that in figure 21 the peaks of σ_a are located somewhere between the peaks and valleys of the TTW. This phase difference is perhaps due to the neglected terms in (5.4).

We now turn to the behaviour of σ_p on the TTW wall, which is plotted in figure 22 at one time instant. The variation of σ_a is also plotted for comparison. Notice that the TTW of relatively small amplitude (and small peaks of σ_a) results in a large-amplitude σ_p. The evolutions of σ_p and $\sigma = \sigma_a + \sigma_p$ over a full period are shown in figures 23 and 24, respectively. Because σ_p is a global effect of the flow, its relation to σ_a is highly nonlinear and complicated. Bearing this in mind, then, it is remarkable to observe that σ_p, and hence the total σ, has the same period as the TTW with an almost

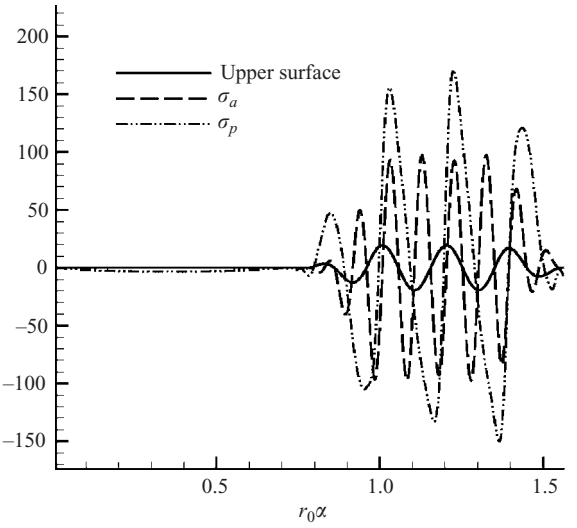

FIGURE 22. σ_a and σ_p of the upper surface of the TTW cylinder at $t = 10.02$. The TTW amplitude is amplified 1000 times.

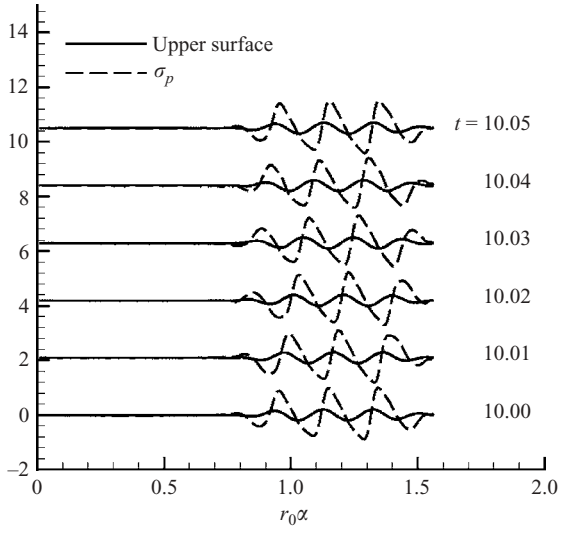

FIGURE 23. σ_p on the upper surface of the TTW cylinder.

locked phase difference. It is this phase-frequency locking that reflects the key physics of FRB (Wu *et al.* 1990): under the optimal condition the flow arrives at a natural periodic state, which does not appear at other arbitrarily chosen conditions. Figure 25 plots the σ_p-variation in space and time on the upper surface of the baseline cylinder and a cylinder with a fixed wavy wall (FWW cylinder) where, in sharp contrast to figure 23, no phase-frequency locking of σ_p to the oscillating flow can be observed. In fact, the FWW cylinder and baseline cylinder have almost the same unfavourable performance: we found that their lift is almost the same, and their drag only differs by 2.2 % (smaller for the FWW cylinder). Similarly, we have found that when the control parameters are far from optimal, the distribution of σ_p on the TTW cylinder may even be quite close to that of the baseline cylinder (figure not shown).

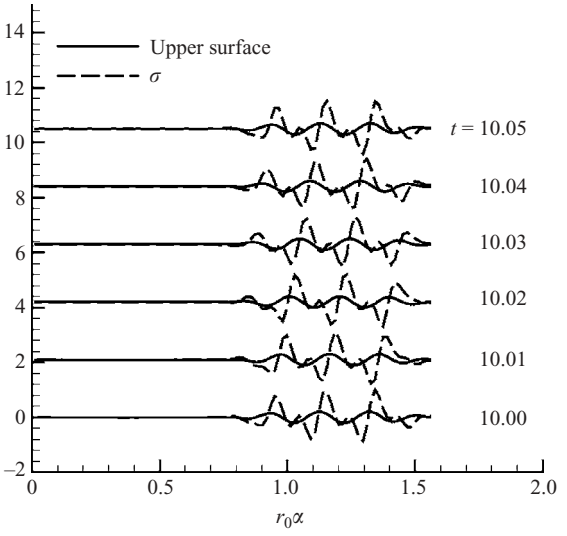

FIGURE 24. $\sigma = \sigma_a + \sigma_p$ on the upper surface of the TTW cylinder.

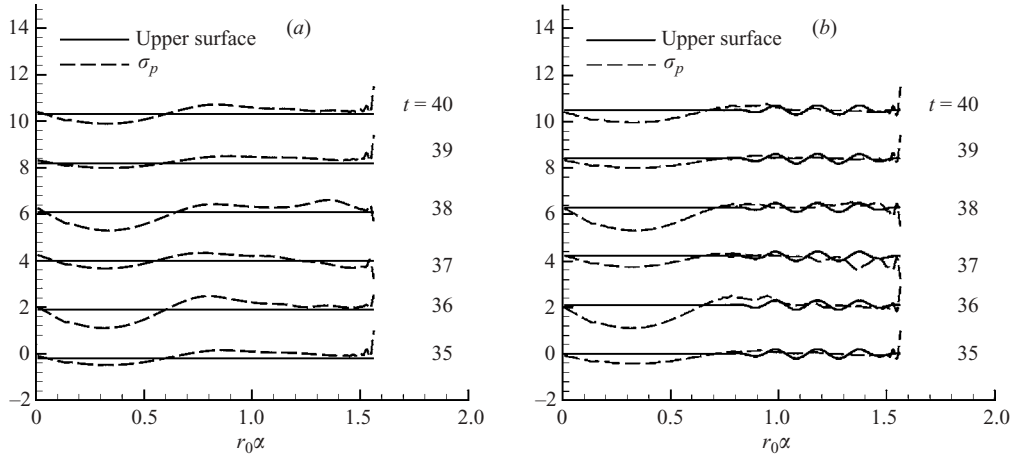

FIGURE 25. σ_p on the upper surface of (*a*) baseline cylinder and (*b*) FWW cylinder.

5.2. *FRB formation by the optimal TTW*

Let us return to figures 22 and 23. Under the optimal condition, we see that the phase difference between σ_p and the TTW is $\pi/2$. The positive σ_p peaks are locked just at the lee side behind each TTW peak, which is the place at which the boundary layer separates to become a free shear layer and roll up into a vortex; on the other hand the negative σ_p peaks are locked just at the windward side of the next TTW peak, which is the place at which the upper portion of the separated shear layer re-attaches. This pattern is the most favourable circumstance for the formation of FRB. Figure 26 supports this assertion, where at each wave trough there is a negative vorticity peak as the on-wall signature of the trapped clockwise vortices. This pattern is different from a clockwise vortex above a rigid wall, below which there must be a boundary layer with positive vorticity. As explained before, the vorticity adjacent to this TTW

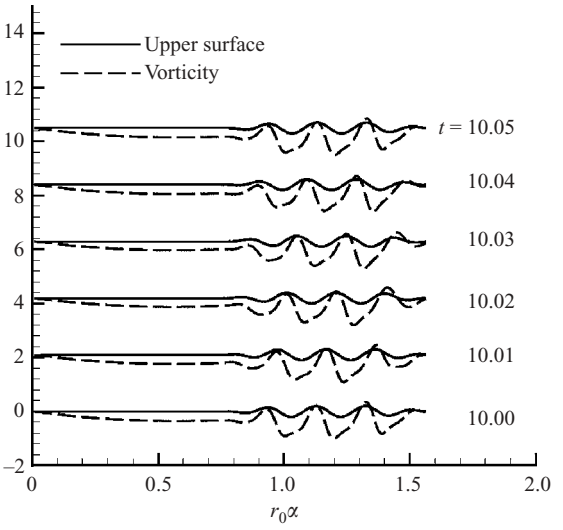

FIGURE 26. Vorticity on the upper surface of the TTW cylinder.

wall can have alternate signs. Figure 26 clearly shows that the dominantly negative vorticity on the TTW wall comes mainly from the upstream attached boundary layer. It can be expected that, should that part of vorticity be removed (say, if the TTW is imposed over the entire cylinder surface), then the on-wall vorticity and skin friction at this optimal condition would have a nearly zero mean, consistent with the prediction of Wu *et al.* (1990). Dynamically, the well-organized FRB flow at this favourable resonant condition is very similar to that of the controlled deep-stalled unsteady separated airfoil flow observed by Wu *et al.* (1998).

5.3. *Independence of the near-wall layer from global flow*

Having compared the detailed characteristics of the TTW-cylinder flow under the optimal FRB condition (naturally periodic) with those of the baseline- or FWW-cylinder flow, we can now answer the following question: why can the TTW wall lead not only to a significant drag reduction but also maintain a global attached flow even under a strong adverse pressure gradient? Although the adverse pressure gradient and associated fluid deceleration still exist over the lee side of the TTW cylinder, they are not 'felt' by the thin fluid layer adjacent to the TTW wall which, if it were adjacent to a rigid wall, would be most vulnerable to the pressure gradient and responsible for the separation. Rather, being sheathed by the FRB, this layer has its own tangential pressure gradient or boundary vorticity flux resonant with the TTW. It maintains its periodicity and amplitude, and is insensitive to the outside pressure variation. The external adverse pressure gradient and associated flow deceleration are only 'felt' by the free fluid layer above the FRB, which however is simply co-moving with the main stream like a potential flow. In other words, while a boundary layer above a rigid wall separates since the external adverse pressure gradient can penetrate all the way down to the wall, this penetration is inhibited by the FRB.

5.4. *Dependence of the TTW wall power consumption on global pressure gradient*

It should be stressed that making the near-wall flow independent of the global adverse pressure gradient by means of an FRB is not without expense. Rather, to produce an FRB for $\partial p/\partial s > 0$ needs a larger power input than that for $\partial p/\partial s = 0$. To see this,

we compare the power consumption of the TTW cylinder with that of an infinitely extended flat plate as the baseline geometry (TTW plate). From (4.5) and (2.2), for the TTW cylinder the integrand of P_{TTW} is

$$-u_r p \cos\phi \, \mathrm{d}s = -2\pi c \frac{A(l)}{\lambda} p \sin\chi \, \mathrm{d}l,$$

the counterpart of which for the TTW plate along the x-direction being

$$-u_y p \cos\phi \, \mathrm{d}s = -2\pi c \frac{A}{\lambda} p \sin\chi \, \mathrm{d}x,$$

where A is constant. Since the preceding discussion has indicated that the oscillating behaviour of $p \sin\chi$ is only scaled to local wave parameters as well as the main-stream velocity above the FRB, in dimensionless form it should be about the same for both flows. Thus, the difference of the power consumptions of the two TTW flows is dominated by that of the amplitudes of their oscillating normal velocities, $\hat{u}_r = cA(l)/\lambda$ and $\hat{u}_y = cA/\lambda$ (dropping the common factor 2π) under their respective optimal conditions. For the TTW plate, Wu *et al.* (1990) found that with a sinusoidal wave of constant $A = 0.2\lambda$, the optimal c/U is 0.414. The main-stream velocity is simply the constant U. Thus, non-dimensionalized by the main-stream velocity above the FRB, we have

$$\frac{\hat{u}_y}{U} = 0.0828 \quad \text{for optimal TTW plate.} \tag{5.5}$$

In contrast, for the TTW cylinder with $N = 4$, by (2.4) the mean amplitude is $\bar{A} = 3\hat{A}/4$, and the main-stream velocity above the FRB, which is the tangential velocity of attached potential flow over the baseline cylinder, varies from $2U$ to zero with a mean $\overline{U} = 4U/\pi$. Thus, given $c/U = 4.0$ and $\hat{A}/\lambda = 0.02d/\lambda = 0.8/\pi$, we have

$$\frac{\hat{u}_r}{\overline{U}} \sim \frac{c\bar{A}}{\overline{U}\lambda} = 0.24 \quad \text{for optimal TTW cylinder,} \tag{5.6}$$

indicating that the power consumption for the TTW cylinder is about 3 times that for the TTW plate.

5.5. *Elimination of vortical wake*

Finally, we further observe that, as shown by figures 24 and 26, under the optimal condition both boundary vorticity flux and boundary vorticity vanish at the downstream end of the TTW wall ($\alpha = \pi$), so no new vorticity is created there and shed into the wake. Meanwhile, as the two rows of vortices of opposite sign travel downstream from upper and lower surfaces, they meet at the trailing edge and cancel each other. Clearly, this behaviour is critical for ensuring a clean and almost irrotational steady downstream flow. In contrast, from figure 25 one sees that at the downstream end of the baseline and FWW cylinders the boundary vorticity flux has alternately positive and negative peaks, indicating an alternate occurrence of flow separation from the upper and lower surfaces, associated with oscillating forces acting on the cylinder and an oscillating vortical wake.

It should be stressed that the wake-free behaviour of optimal TTW flow appears not only when the flow is symmetric with respect to the x-axis but also for flows without this symmetry. In the TTW airfoil flow at stall angle of attack reported in Wu *et al.* (2003), the TTW was generated only on a portion of the upper surface, but the flow is still wake-free, in contrast to the periodic vortex shedding from a rigid airfoil at the same angle of attack. The underlying mechanism of this behaviour deserves further exploration.

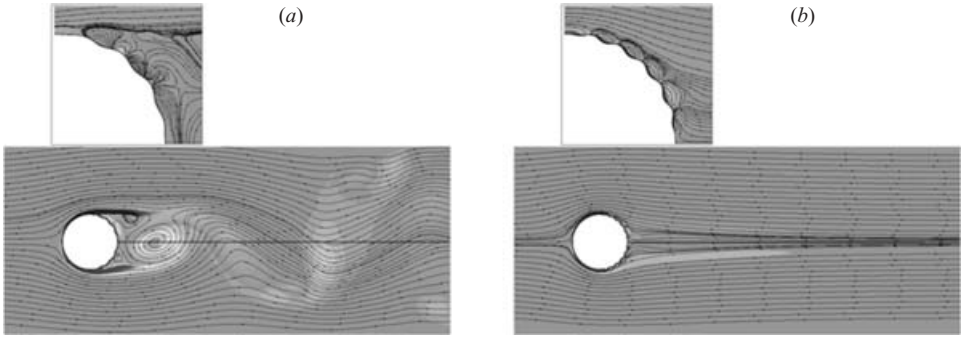

FIGURE 27. Control effect with different wavenumbers at $Re = 500$, $c = 4$, $a = 0.01$, $t = 50$, and (*a*) $N = 4$, (*b*) $N = 6$.

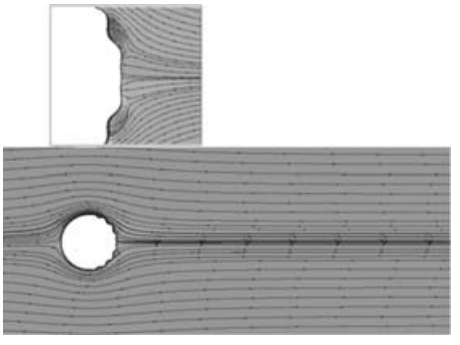

FIGURE 28. FRB control effect at $Re = 2000$, $c = 4$, $a = 0.02$, $n = 4$ and $t = 20$.

6. Dependence of FRB control on control parameters and Reynolds number

The preceding discussion is based on the results of a single case. Here we present the numerical results of several typical cases to show the dependence of the FRB control on wave parameters and the Reynolds number. We have found that with larger wave speed c, the control effect is better, but requires more power input. Therefore, we seek the optimal parameters at the minimum c.

6.1. *Wavenumber effect at* $Re = 500$

Figure 27 shows that, for smaller wave amplitude ($a = 0.01$) with $c = 4$ at $Re = 500$ and $t = 20$, the choice of wavenumber N has a strong effect on the controlled flow behaviour. Too few waves (figure 27*a*) cannot suppress the vortex shedding, but good control effect can be achieved with larger N (figure 27*b*).

6.2. *Reynolds number effect*

Figure 28 shows the flow pattern at $Re = 2000$ for $c = 4$, $a = 0.02$, $N = 4$ at $t = 20$. The FRB control effect is similar to that at $Re = 500$. A further increase of Re to 5000, see figure 29, may still produce good control until $t = 5$, but small vortices appear in the wake near the rear stagnation point at $t = 10$ and $t = 20$.

However, at this Re, if N is increased to 6 with $a = 0.01$, figure 30 indicates that although at $t = 5$ small wake vortices appear near the rear stagnation point, shedding is not enhanced at later times.

Therefore, we may conclude that (i) larger wave speeds produce better control, but need larger power input; (ii) at the same wave speed, decreasing the wave amplitude

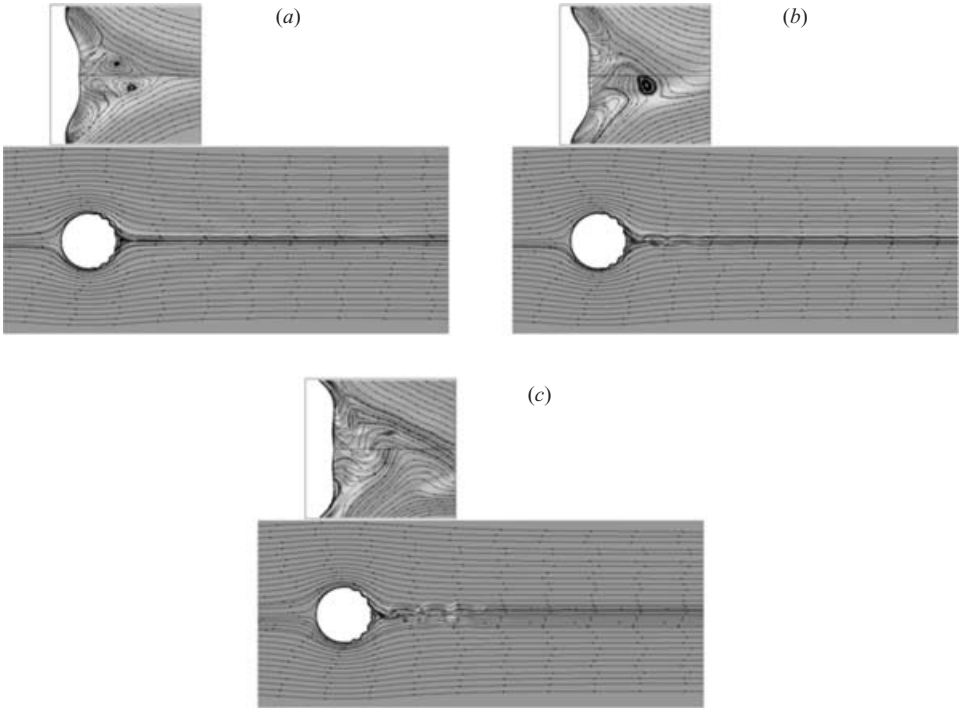

FIGURE 29. FRB control effect at $Re = 5000$, $c = 4$, $a = 0.02$ and $N = 4$ for different times: (*a*) $t = 5$, (*b*) $t = 10$, (*c*) $t = 20$.

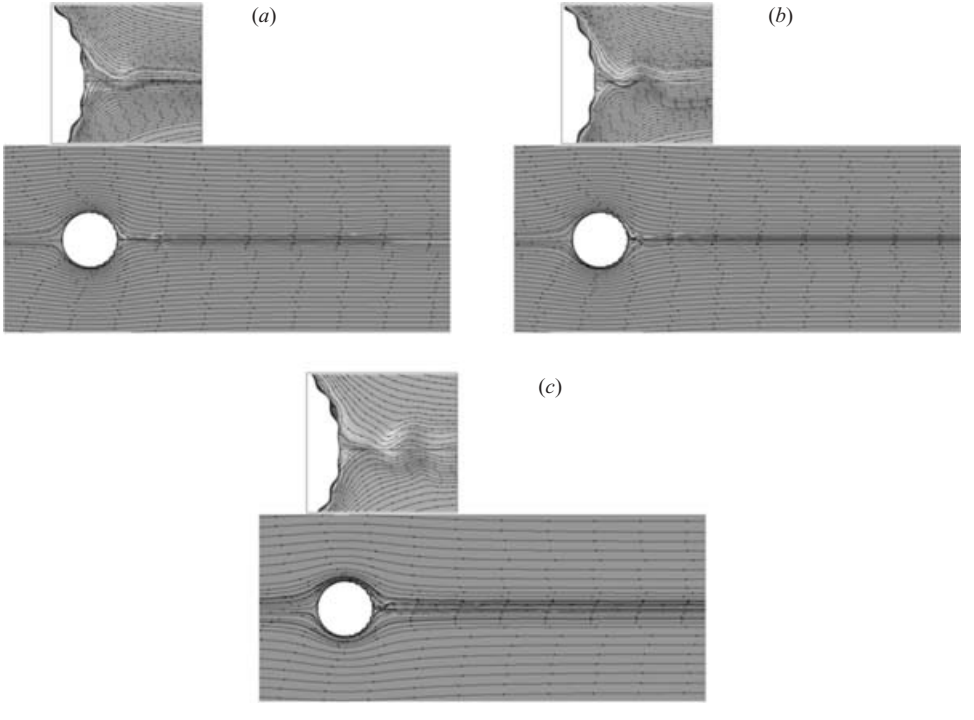

FIGURE 30. FRB control effect at $Re = 5000$, $c = 4$, $a = 0.01$, and $N = 6$ at different times: (*a*) $t = 5$, (*b*) $t = 10$, (*c*) $t = 20$.

but increasing the wavenumber can achieve good control; (iii) a/λ cannot be too small, thus for good control, if a is reduced so should λ; and (iv) over a quite wide range of the Reynolds number, good control can be achieved by choosing appropriate wave parameters.

7. Concluding remarks

This numerical study demonstrates that, as an advanced use of moving-wall flow control, a properly generated transverse travelling wave (TTW) on a flexible wall can effectively eliminate the spontaneous unsteady flow separation from a circular cylinder under a strong adverse pressure gradient. The control makes the global flow almost fully attached except in the local controlling region, with a clean, steady and irrotational downstream part. The drag is significantly reduced, and the oscillating side force is completely suppressed. The hydrodynamic power input for activating the TTW is smaller than the power saving due to drag reduction. Along with the study of Wu *et al.* (2003), this work indicates that the TTW control strategy is in principle applicable to bluff-body flow control in a quite wide range of Reynolds numbers. As the development of smart flexible material, artificial muscle and control techniques proceeds, the TTW control could become increasingly important.

The basic mechanism of the TTW control is the fluid roller bearing (FRB) consisting of a row of vortices trapped by each wave trough. They are formed by the rolling up of free shear layers separating from the lee side of each wave peak, which occurs if the TTW amplitude is sufficiently large to ensure local separation and if the Reynolds number based on the wavelength is also sufficiently large (above 100). In between the FRB and the TTW wall the thin fluid layer is scaled to the local wavelength and frequency of the TTW, but independent of the global scales. The FRB serves as a sheath to effectively inhibit the momentum–energy exchange between the flow adjacent to the wall and that in the main stream. Therefore, the global adverse pressure gradient on the lee side of the cylinder no longer influences the near-wall flow, and the common root cause of flow separation is removed. The symmetric arrangement of the TTW on the upper and lower surfaces ensures that the vortices in FRB cancel each other as they propagate into the wake, but this wake-free behaviour also appears in asymmetric TTW flow. However, this insensitivity of the near-wall layer to the global flow is reached at the cost that more power input is needed for actuating the optimal TTW flow under an adverse pressure gradient than that without a pressure gradient.

The FRB effect occurs only at certain optimal conditions, in particular a critical range of the wave speed c/U. Under such a condition, the pressure gradient along the TTW wall or boundary vorticity flux is in resonance with the TTW. Its phase and frequency are locked to that of the TTW, and its positive and negative peaks are at the correct places on the wavy wall to promote the desired flow separation and reattachment. Once established, this resonance appears seems to form a closed-loop favourable feedback system to stabilize the FRB. However, so far no theory can predict the optimal parameter combination.

There are still many issues to be addressed. A predictive theory for the optimal parameter combination for TTW on a curved wall and at an adverse pressure gradient is desirable. The stability characteristics of the FRB flow need to be explored. More advanced numerical schemes are needed to extend the calculation to a larger Reynolds-number range with higher accuracy. An experiment with a TTW flexible wall has long been awaited. Above all, how the FRB would behave in three-dimensional flow

is still completely unknown. If all these issues could be solved, one would be in the position to see whether the role of the conventional boundary layer ('fluid sliding bearing') could eventually be replaced by the controlled FRB.

This work was supported in part by the National Science Foundation of China (10172095, 10172006, 10572005) and the Key project of Natural Science Foundation of Jiangsu (BK2003208). Our deep appreciation goes to Professor George F. Carnevale of Scripps Institution of Oceanography, USA, for detailed comments, to Professors James M. Wu and Xiao Ming for providing figure 4, to Ms Feng-Rong Zhu for the preparation of several figures, and to referees for their valuable suggestions.

REFERENCES

Bergmann, M., Cordier, L. & Brancher, J.-P. 2006 On the generation of a reverse von Kármán street for the controlled cylinder wake in the laminar regime. *Phys. Fluids* **18**, 028101.

Ferziger, J. H. & Perić, M. 1999 *Computational Method for Fluid Dynamics*. Springer.

Hertel, H. 1966 *Structure-Form-Movement*. Reinhold Publishing Co., NY, 1963 (English transl. 1966).

Ho, C. M. & Huerre, P. 1984 Perturbed free shear layers. *Annu. Rev. Fluid Mech.* **16**, 365–424.

Karniadakis, G. E. & Choi, K. S. 2003 Mechanisms on transverse motions in turbulent wall flows. *Annu. Rev. Fluid Mech.* **35**, 45–62.

Kim, J., Kim, D. & Choi, H. 2001 An immersed-boundary finite-volume method for simulations of flow in complex geometries. *J. Comput. Phys.*, **171**, 132–150.

Lai, M. & Peskin, C. S. 2000 An immersed boundary method with formal second-order accuracy and reduced numerical viscosity. *J. Comput. Phys.*, **160**, 705–719.

Modi, V. J. 1997 Moving surface boundary-layer control: A review. *J. Fluids Struct.* **11**, 627–633.

Modi, V. J. 2000 On the moving surface boundary-layer control. *AIAA Paper* 2000-2238.

Patnaik, B. S. V. & Wei, G. W. 2002 Controlling wake turbulence. *Phys. Rev. Lett.* **88**, 054502.

Roshko, A. 1993 Perspectives on bluff body aerodynamics. *J. Wind Ind. Aerodyn.* **49**, 70–100.

Savchenko, Y. N. 1980 Hydrodynamics effects of a traveling wave. *USSR Bionics. Trans.* **JPRS L**/9420.

Taneda, S. 1978 Visual study of unsteady separated flows around bodies. *Prog. Aerospace Sci.* **17**, 287–348.

Tseng, Y.-H. & Ferziger, J. H. 2003 A ghost-cell immersed boundary method for flow in complex geometry. *J. Comput. Phys.* **192**, 593–623.

Williamson, C. H. K. 1996 Vortex dynamics in the cylinder wake. *Annu. Rev. Fluid Mech.* **28**, 477–539.

Wu, C. J., Xie, Y. Q. & Wu, J. Z. 2003 "Fluid Roller Bearing" effect and flow control. *Acta Mechenica Sinica* **19**(5), 476–484.

Wu, J. M., Wu, J. Z., Wu, C. J. & Vakili, A. D. 1990 Preliminary study of nonlinear flow over traveling wavy wall. In *Nonsteady Fluid Dynamics* (ed. J. A. Miller & D. P. Telionis). pp. 359–368. Philadelphia: SIAM.

Wu, J. Z., Lu, X. Y., Denny, A. G., Fan, M. & Wu, J. M. 1998 Post-stall flow control on an airfoil by local unsteady forcing. *J. Fluid Mech.* **371**, 21–58.

Wu, J. Z., Pan, Z. L. & Lu, X. Y. 2005*a* Unsteady fluid dynamic force solely in terms of control-surface integral. *Phys. Fluids* **17**, 098102.

Wu, J. Z., Vakili, A. D. & Wu, J. M. 1991 Review of the physics of enhancing vortex lift by unsteady excitation. *Prog. Aerosp. Sci.* **28**, 73–131.

Wu, J. Z. & Wu, J. M. 1996 Vorticity dynamics on boundaries. In *Advances in Applied Mechanics 32* (ed. J. H. Huchinson & T. Y. Wu), pp. 119–275. Academic.

Wu, J. Z., Wu, X. H. & Wu, J. M. 1993 Streaming vorticity flux from oscillating walls with finite amplitude. *Phys. Fluids* A **5**, 1933–1938.

Wu, J. Z., Yang, Y. T., Luo, Y. B. & Pozrikidis, C. 2005*b* Fluid kinematics on a deformable surface. *J. Fluid Mech.* **541**, 371–381.

Wu, X. H., Wu, J. Z. & Wu, J. M. 1991 Streaming effect of rapid wall oscillation to boundary layer separation. *AIAA Paper* 91-0545.

Yang, Z. & Wu, J. Z. 2005 Drag reduction by axisymmetric traveling wavy wall. *J. Univ. Sci. Tech. China* **35**, 471–479.

Zdravkovich, M. M. 1997 *Flow Around Circular Cylinders. Vol. 1: Fundamentals*. Oxford University Press.

Zdravkovich, M. M. 2002 *Flow Around Circular Cylinders. Vol. 2: Applications*. Oxford University Press.

Zhao, H., Wu, J. Z. & Luo, J. S. 2004 Turbulent drag reduction by traveling wave of flexible wall. *Fluid Dyn. Res.* **34**, 175–198.

Zhou, M. D. 1992 Separation, shear layer instability and their control. UTSI Short Course Series "High Angle of Attack/Unsteady Flow Phenomena, University of Tennessee Space Institute, Tullahoma.